agronomy

MDPI

Article

Multitemporal UAV-Based Estimation of Kenaf (*Hibiscus cannabinus* L.) Plant Height Under Nitrogen and Compost Treatments

TaekJin Yoon [1], TaeWan Kim [1,*] and SungYung Yoo [2,*]

[1] School of Plant Resources and Landscape Architecture, Hankyong National University, Anseong 17579, Republic of Korea; yoonshark97@hknu.ac.kr
[2] Institute of Ecological Phytochemistry, Hankyong National University, Anseong 17579, Republic of Korea
* Correspondence: taewkim@hknu.ac.kr (T.K.); lsn136@hknu.ac.kr (S.Y.); Tel.: +82-10-6292-3896 (T.K.); +82-10-4938-6825 (S.Y.)

Abstract

This study aimed to evaluate the growth responses of kenaf (*Hibiscus cannabinus* L.) under nitrogen and compost treatments and to develop a UAV-based plant height estimation model. Ground-measured plant height differences were not significant at harvest (110 days after sowing, DAS), highlighting the need for multitemporal monitoring. Multispectral drone imagery was acquired at five growth stages (20–110 DAS). Object-based image segmentation was applied to extract pure vegetation areas, and digital surface model differencing (ΔDSM_t) was used to reduce micro-topographic effects. A UAV-based multiple linear regression (UAV-MLR) model was developed using ΔDSM_t, NDVI, GNDVI, and NGRDI to integrate complementary structural and spectral information. Evaluated on the calibration dataset, the UAV-MLR model demonstrated high fitting performance (adjusted R^2 = 0.9858, RMSE = 14.95 cm, MAE = 11.31 cm), outperforming the ground-based simple linear regression (G-SLR) model based on stem diameter (adjusted R^2 = 0.9615, RMSE = 39.68 cm, MAE = 29.16 cm). By integrating structural and spectral information, the proposed approach reduced RMSE by 62.3%, offering a highly accurate, non-destructive tool for crop monitoring and precision agriculture.

Keywords: kenaf; UAV remote sensing; plant height; digital surface model; vegetation indices; multiple linear regression

Academic Editor: Alberto San Bautista

Received: 15 July 2026
Revised: 31 August 2026
Accepted: 10 September 2026
Published: 14 September 2026

1. Introduction

Recent global concerns over climate change have highlighted the need to mitigate environmental impacts and transition toward precision agriculture based on low-input farming technologies [1–6]. Kenaf (*Hibiscus cannabinus* L.) is a representative high-yield crop known for its superior biomass productivity [7,8] and exceptionally high carbon dioxide (CO_2) uptake capacity compared with conventional crops [9,10]. It is a subtropical annual crop native to Africa, characterized by a short growth period of approximately 100–125 days and rapid growth, reaching up to 4–6 m in height [11,12]. As the economic and environmental value of kenaf has increased, diverse studies have focused on its sustainable production, particularly given its ability to maintain stable growth with relatively low inputs of chemical fertilizers and pesticides [13,14]. This makes kenaf well suited for low-input precision agriculture.

However, the structural development and biomass accumulation of kenaf are strongly governed by nutrient availability, particularly soil nitrogen and organic compost applications. Varied fertilization regimes can induce marked spatial and temporal variation in plant height and canopy spectral characteristics [15,16]. Moreover, as the crop transitions to reproductive development after flowering, vertical stem elongation slows, and treatment-induced height differences tend to converge by the final harvest stage [17,18]. This physiological shift limits the diagnostic value of single-point height measurements at harvest and underscores the need for multitemporal monitoring across the entire crop lifecycle to accurately evaluate fertilization responses [19,20].

Conventional crop growth assessment still relies on direct field measurements of growth indicators such as plant height and stem diameter, which requires substantial labor and time and can reduce the reliability of results depending on the operator's skill and weather conditions [21–23]. For crops such as kenaf, which grow tall and are planted at high density, field accessibility and survey efficiency decline markedly as the crop enters later growth stages, creating physical limitations for manual growth measurements. Furthermore, as a bast fiber crop, kenaf exhibits a distinct developmental asynchrony; while vertical height elongation slows after flowering, radial stem thickening continues as assimilates are redistributed to structural stem tissues [24,25]. Consequently, traditional ground-based regression models (G-SLR) that rely solely on the allometric relationship between stem diameter and plant height may become less reliable in late growth stages [26]. Because canopy height in kenaf is a key indicator for estimating biomass and carbon storage, there is a need to introduce non-destructive surveying techniques that can monitor the entire growth cycle.

Recently, with the rapid advancement of the Fourth Industrial Revolution, remote sensing technology using unmanned aerial vehicles (UAVs) has continued to develop, and vegetation monitoring techniques that are less constrained by time and space and are highly cost-effective are being applied in agriculture [27–29]. UAVs have the advantage of acquiring high-resolution imagery for small-scale or site-specific cultivation areas according to the user's purpose [30]. In particular, the use of drones equipped with multispectral sensors has made it possible to directly apply various vegetation monitoring methods originally developed on the basis of satellite imagery to crop-level precision analysis [31–35]. In addition, the generation of a digital surface model (DSM) through photogrammetric techniques enables the acquisition of three-dimensional physical structural information on crops [19,36,37].

Despite these advantages, for crops such as kenaf that are tall and structurally complex, there are limitations to precisely estimating actual canopy height using imagery from a single time point alone [38], and it is especially difficult to accurately reflect growth changes because of the effects of terrain variability and reference elevation [39,40]. Traditional single-temporal DSM calculations are often distorted by micro-topographical variations across the field [40,41]. Moreover, early-stage drone observations often suffer from mixed-pixel interference, where young crop canopies are spectrally and spatially confounded by surrounding soil and non-target vegetation background, distorting spectral vegetation indices [42,43]. To overcome these limitations, recent studies have highlighted the importance of multitemporal baseline correction in canopy height estimation and object-based image processing to isolate pure vegetation and reduce background noise [44,45].

To address these critical research gaps, the present study compared ground-based growth measurements with UAV-derived multispectral and structural variables across multiple growth stages to examine the potential of UAV data for plant height estimation in kenaf under diverse fertilization treatments. Specifically, this study aimed to (1) implement an object-based preprocessing workflow to isolate pure crop vegetation and reduce soil and non-target background noise, (2) construct a baseline-corrected canopy height model (ΔDSM_t) through multitemporal digital surface model subtraction to reduce micro-topographic errors, and (3) develop a UAV-based multiple linear regression (UAV-MLR) model using standardized spectral and structural parameters while rigorously comparing its fitting performance with a conventional ground-survey-based regression model across multiple growth stages.

2. Materials and Methods

2.1. Experimental Design and Kenaf Cultivation

This study was conducted on kenaf (*Hibiscus cannabinus* L.) cultivated in an upland field at the experimental farm of Hankyong National University (37°0′42.31″ N, 127°19′12.48″ E). The cultivation area (Figure 1) was approximately 300 m², consisting of 24 plots (3 m × 3 m each) with three independent replicates for each of the eight fertilizer treatments. Plant spacing was maintained at 20 cm × 20 cm (row × plant). Sowing was carried out on 18 June 2025, and the crop was grown until 5 October 2025 (110 days after sowing, DAS).

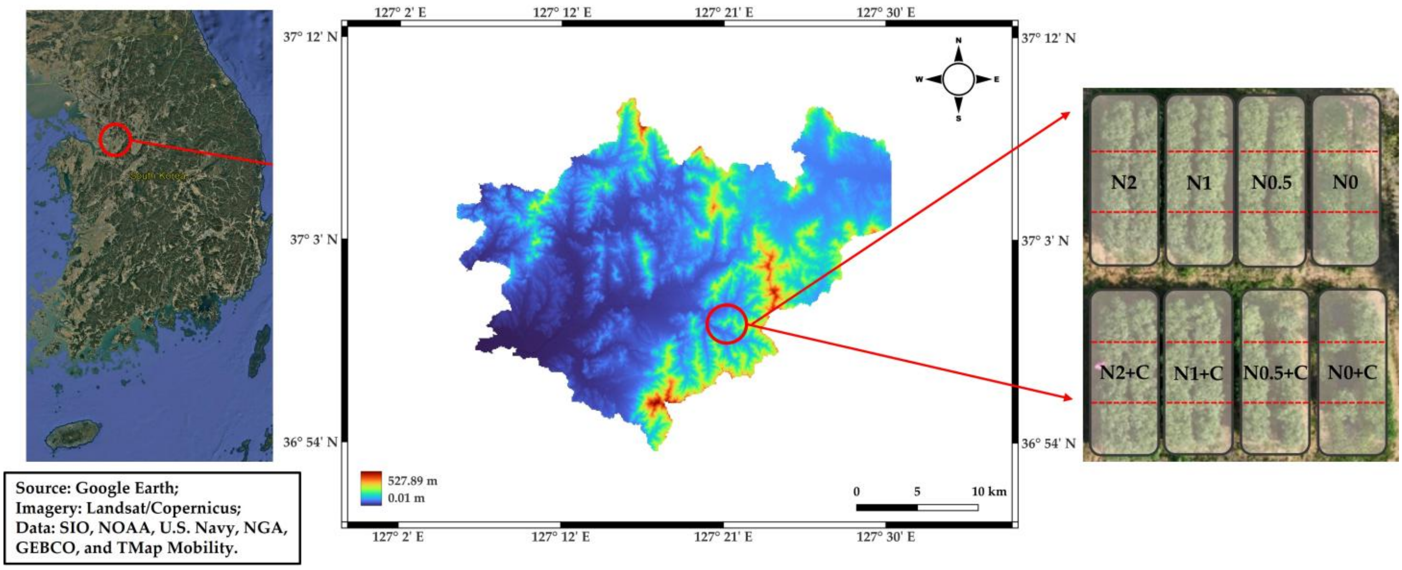

Figure 1. Geographic location of the study site in Anseong, South Korea, and spatial layout of the experimental field. The map details the regional location and spatial layout of the 24 experimental plots, highlighting the eight fertilizer treatments (N0, N0.5, N1, N2, N0+C, N0.5+C, N1+C, and N2+C), with individual plot boundaries delineated by red dashed lines on the cropped UAV orthomosaic. The treatments were arranged to evaluate the combined effects of nitrogen fertilization rate and compost application (Table 1). The N0 treatment received no mineral fertilizer, the N0+C treatment received compost only, and the remaining treatments received the assigned nitrogen rates with basal phosphorus and potassium application. The satellite image in the left panel was obtained from Google Earth (imagery: Landsat/Copernicus; data: SIO, NOAA, U.S. Navy, NGA, GEBCO, and TMap Mobility).

Table 1. Summary of the fertilizer treatments used in this study.

Treatment	Basal N (kg ha^{-1})	Top-Dressing N (kg ha^{-1})	Total N (kg ha^{-1})	Compost (kg ha^{-1})
N0	0.0	0.0	0.0	0.0
N0+C	0.0	0.0	0.0	20,000
N0.5	24.25	24.25	48.5	0.0

N0.5+C	24.25	24.25	48.5	20,000
N1	48.5	48.5	97.0	0.0
N1+C	48.5	48.5	97.0	20,000
N2	97.0	97.0	194.0	0.0
N2+C	97.0	97.0	194.0	20,000

Note: Phosphorus (P_2O_5) and potassium (K_2O) were applied as basal fertilizer only to the mineral fertilizer-treated plots (N0.5, N0.5+C, N1, N1+C, N2, and N2+C) at fixed rates of 102.0 kg ha^{-1} and 58.0 kg ha^{-1}, respectively, according to the Rural Development Administration (RDA) standard recommendations.

Mineral fertilizer was applied one week before sowing at a standard rate recommended by the Rural Development Administration (97 kg N, 102 kg P_2O_5, 58 kg K_2O ha^{-1}) [46]. Nitrogen was applied in equal proportions as basal and top-dressing fertilizer (50:50), with top-dressing applied at 40 DAS.

The compost used in this study was a livestock manure compost (Daelim Fertilizer, Yeoju, Republic of Korea), containing more than 30% organic matter, 50% poultry manure, 10% swine manure, and the remainder sawdust. Compost was applied one week before sowing at a rate of 20,000 kg ha^{-1} and the application amount was adjusted according to each plot area.

2.2. Ground Truth Data Collection

To validate the UAV-based estimation model and construct a comparative control model based on conventional growth measurements, ground surveys were conducted on the same dates as UAV image acquisition (20, 40, 60, 80, and 110 DAS). Specifically, at 40 DAS, all ground survey measurements were performed prior to the application of nitrogen top-dressing to evaluate the baseline crop growth state.

For each treatment plot, plants were randomly selected for measurement (n = 5 per treatment at 20 and 40 DAS; n = 3 per treatment at 60 and 110 DAS; n = 4 per treatment at 80 DAS). The sample sizes in the later growth stages were adjusted due to mid-stage destructive sampling and the exclusion of plants damaged by field conditions (e.g., severe lodging or stem breakage in late stages).

Plant height was manually measured using a measuring tape (KMC-86, Komelon Corporation, Republic of Korea) from the soil surface to the apex of the main stem. At the same time, stem diameter was measured at 15 cm above the basal stem portion using a digital caliper (CD-15APX, Mitutoyo Corporation, Japan; precision, ±0.02 mm).

Across the eight treatments, a total of 160 individual plant measurements were collected across the five survey dates.

For ANOVA and mean comparisons, all individual plant measurements (n = 160) were used to preserve plant-to-plant variability. For regression modeling (G-SLR and UAV-MLR), the measurements of the selected plants per treatment were averaged to obtain representative treatment means (n = 8 per survey date; n = 40 in total across all five survey dates). The ground-measured dataset was used to develop the Ground-based simple linear regression model (G-SLR) and as ground truth for validating the UAV-based multiple linear regression model (UAV-MLR).

2.3. UAV Multispectral Image Acquisition and Orthomosaic Generation

To monitor seasonal growth changes in kenaf, image acquisition was carried out at 20, 40, 60, 80, and 110 DAS using a multispectral drone (Mavic 3 Multispectral Enterprise, DJI, China) equipped with an RGB camera and a multispectral camera (with the 40 DAS flight mission conducted prior to top-dressing). This platform captures digital images in three RGB bands (Blue = R445, Green = R545, and Red = R650) and is also equipped with a multispectral sensor payload capable of acquiring four single-waveband channels: Green (R560 ± 16), Red (R650 ± 16), Red-edge (R730 ± 16), and Near-Infrared (R860 ± 26). Drone imaging was conducted under clear, cloudless weather conditions between 11:00 a.m. and 12:00 p.m., when plant photosynthesis is most active and shading effects can be minimized.

For mapping the experimental field, an automatic flight mission was configured using the DJI Pilot 2 app (ver. 17.3.0.21), and the main imaging conditions were as follows:

- Flight altitude: 12 m (GSD = 0.55 cm/pixel);
- Flight speed: 1 m/s;
- Image overlap: 80% front overlap and 70% side overlap;
- Capture mode: time-interval shooting;
- Positioning accuracy: RTK GNSS network service;
- RTK positioning status: Status 50 (Fixed solution, cm-level accuracy) maintained throughout all flights.

Under the above conditions, each flight collected 60 RGB images and 240 Multispectral images.

The collected RGB images were aligned using WebODM (ver. 3.4.0) [47] to generate a digital surface model (DSM) and an orthomosaic (Figure 2). The processing quality results were as follows:

- Average GSD: 0.8 cm;
- GPS RMS Error: 0.027 m (X: 0.015 m, Y: 0.020 m, Z: 0.011 m);
- Horizontal Accuracy (CE90): 0.033 m;
- Vertical Accuracy (LE90): 0.020 m.

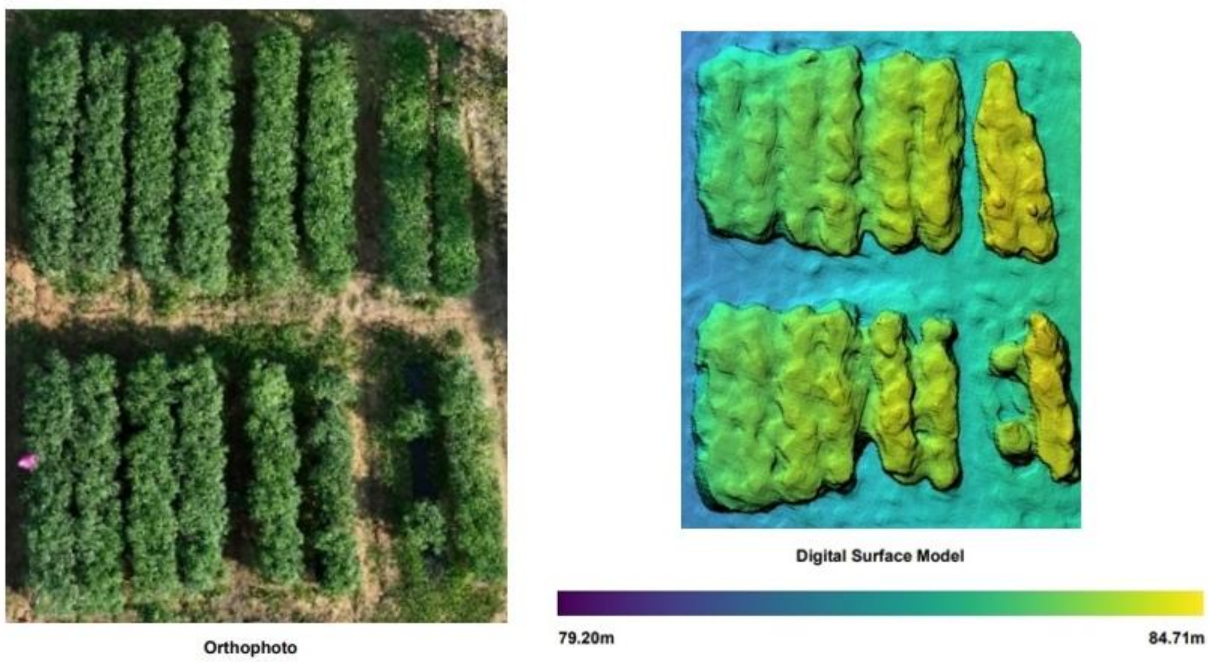

(a) (b)

Figure 2. High-resolution UAV mapping products from WebODM 3.4.0 processing of 60 RGB images (GSD: 0.8 cm, LE90: 0.020 m): (**a**) orthomosaic showing kenaf treatment plots (60 DAS); (**b**) Digital Surface Model (DSM) visualizing canopy height variation (60 DAS).

2.4. Metadata-Based Radiometric Calibration and Spectral Reflectance Calculation

Radiometric calibration was performed to convert the raw digital numbers (DNs) of the acquired single-waveband images into spectral reflectance, which is a physical unit required for accurate spectral reflectance calculation. This process was automatically carried out through the WebODM pipeline in accordance with the DJI Enterprise image processing guide [48], and the metadata structure is as follows.

First, dark current noise was removed from the raw pixel values recorded by the sensor, and band-specific spectral radiance L was derived by accounting for the exposure parameters and sensor temperature (Equation (1)).

$$L(\lambda) = V(x,y) \times \frac{a_1 \times (DN - DN_{black})}{g \times t \times (a_2 \times T + a_3)} \quad (1)$$

- $L(\lambda)$: band-specific spectral radiance ($W \times m^{-2} \times sr^{-1} \times \mu m^{-1}$);
- $V(x,y)$: pixel-wise polynomial-model-based vignetting correction function embedded in the XMP metadata;
- DN_{black}: sensor dark current noise (Black Level);
- a_1, a_2, a_3: sensor-specific calibration coefficients;
- g: Sensor Gain;
- t: Exposure Time (μs);
- T: sensor operating temperature (°C).

Second, the derived radiance L values were combined with irradiance measurements recorded in real time by the downwelling light sensor (DLS) mounted on the top of the aircraft, as well as the aircraft attitude information from the inertial measurement unit (IMU) and the solar elevation angle, to calculate pure spectral reflectance ρ with atmospheric and environmental effects removed (Equation (2)).

$$\rho(\lambda) = \frac{\pi \times L(\lambda)}{E_{sensor}(\lambda) \times f(\theta, \phi)} \quad (2)$$

- $\rho(\lambda)$: final spectral reflectance values (0–1);
- $E_{sensor}(\lambda)$: solar irradiance measured by the downwelling light sensor (DLS) mounted on the drone;
- $F(\theta,\Phi)$: cosine incidence-angle correction coefficient considering the solar zenith angle (θ), solar azimuth angle (Φ), and the drone's flight attitude angles.

2.5. Extracting Vegetation Features and Canopy Height Modeling

Vegetation indices, including NDVI, GNDVI, GLI, NGBDI, NGRDI, and VARI, were calculated using the Raster Calculator in QGIS (ver. 3.42.1) [49] based on the calibrated multispectral reflectance layers and RGB images (Table 2).

Table 2. List of UAV-derived vegetation indices used for multiple linear regression modeling in this study.

Index	Description	Formula	References
NDVI	Normalized Difference Vegetation Index	(RNIR − RRED)/(RNIR + RRED)	[50]
GNDVI	Green Normalized Difference Vegetation Index	(RNIR − RGREEN)/(RNIR + RGREEN)	[51]
GLI	Green Leaf Index	$(2 \times R_G - R_R - R_B)/(2 \times R_G + R_R + R_B)$	[52]
NGBDI	Normalized Green Blue Difference Index	$(R_G - R_B)/(R_G + R_B)$	[42]
NGRDI	Normalized Green Red	$(R_G - R_R)/(R_G + R_R)$	[53]

	Difference Index		
VARI	Visible Atmospherically Resistant Index	$(R_G - R_R)/(R_G + R_R - R_B)$	[43]

Note: RNIR, RRED, RGREEN represent the reflectance bands from the multispectral sensor; R_R, R_G, R_B represent the digital values from the calibrated RGB sensor.

After that, a region of interest (ROI) polygon layer defining the plot boundaries was manually created to remove soil background and shadow noise, and the raster was clipped using this ROI layer. The clipped raster was then converted into pixel-based vector objects through a raster-to-polygon transformation, while the raster values of individual pixels were preserved as attribute values (Figure 3a).

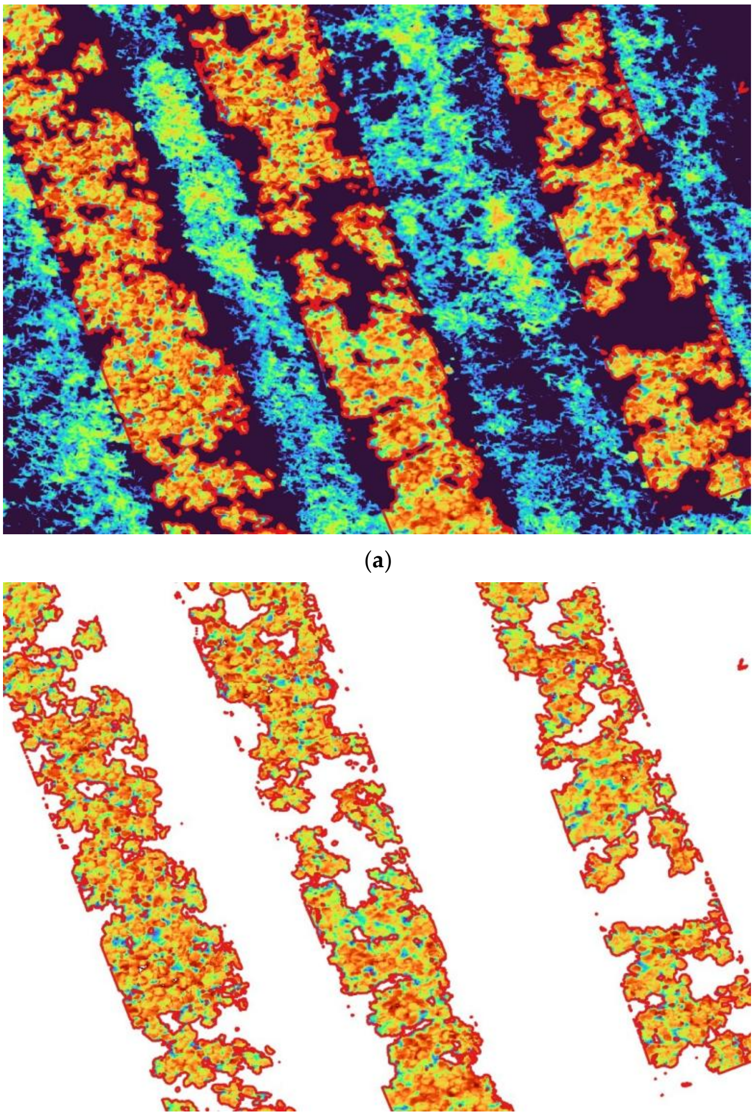

(**a**)

(**b**)

Figure 3. Object-based vegetation extraction and canopy boundary delineation workflow: (**a**) ROI-defined plot clipping from the original vegetation indices raster; (**b**) raster-to-polygon vectorization of the clipped raster for extracting plot-level canopy boundaries.

To preserve the morphological integrity of individual plants and prevent boundary distortion in the vector objects, the 8-connected component labeling (CCL) algorithm, which merges adjacent pixels into a single continuous object, and the Moore-neighbor contour tracing algorithm were sequentially applied. Through this process, individual pixel polygons were integrated into a single intact vector polygon object, thereby constructing a plot-level vegetation-only mask layer (Figure 3b).

At early growth stages, when plant canopies were small and spatially separated, the CCL and contour tracing procedures often produced distinct vector objects corresponding to individual plants. As the canopies developed and overlapped at later stages, adjacent vegetation pixels were merged into single connected components, resulting in effectively plot-level vegetation masks. For all subsequent analyses, vegetation pixels within each plot mask were aggregated to compute plot-level statistics (e.g., mean vegetation index values and mean canopy height).

Figure 4 illustrates the process of constructing a relative canopy height model (ΔDSM_t) through DSM subtraction from the pre-sowing stage to the late growth stage. To quantitatively estimate physical changes in kenaf canopy height, a reference digital surface model obtained under the same flight conditions in the bare-soil state before sowing was first generated (16 June 2025; DSM_{pre}; Figure 4a). Then, the relative canopy height model for each growth stage (e.g., 60 DAS on 17 August 2025; DSM_t; Figure 4b) was derived by subtracting the reference bare-soil surface model from the surface model acquired at each growth stage (ΔDSM_t; Figure 4c) (Equation (3)).

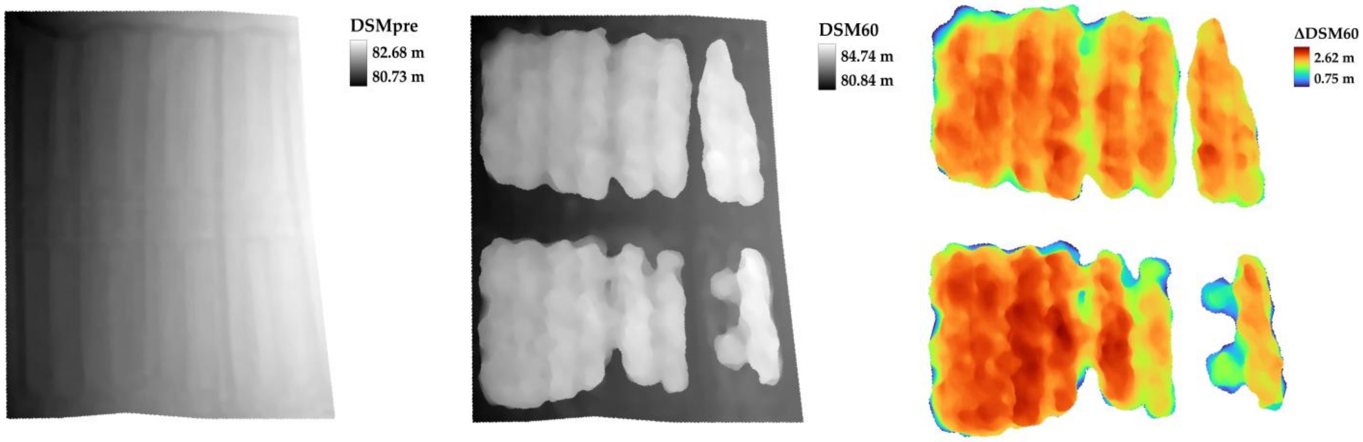

(**a**) (**b**) (**c**)

Figure 4. Workflow for generating the relative canopy height model (ΔDSM_t) through digital surface model subtraction: (**a**) baseline topography under bare soil conditions (DSM_{pre}, 16 June 2025; vertical accuracy LE90 = 0.021 m); (**b**) absolute elevation data of the field during the mid-growth stage at 60 DAS (DSM_t, t = 60, 17 August 2025; vertical accuracy LE90 = 0.019 m); (**c**) subtracted relative canopy height model ($\Delta DSM_t = DSM_t - DSM_{pre}$) with pure vegetation masking.

The relative canopy height model was calculated as:

$$\Delta DSM_t = DSM_t - DSM_{pre} \quad (3)$$

The zonal statistics analysis was performed using the derived plant-object polygon layer, and the mean vegetation index values and mean ΔDSM_t values within the pure vegetation areas of each plot were extracted as the final independent variables.

2.6. Statistical Analysis

Differences in kenaf growth characteristics according to fertilizer treatment were tested using a two-way ANOVA, with nitrogen fertilizer level and compost application as fixed effects, based on all individual plant measurements (n = 1). Mean comparisons among treatments were performed using Duncan's multiple range test, and significance levels were set at $p < 0.05$, $p < 0.01$, $p < 0.001$.

https://doi.org/10.3390/agronomy16181805

A simple linear regression model using conventional ground survey variables and a multiple linear regression model using processed drone data were separately developed using the treatment mean dataset (n = 40) to compare their performance in predicting kenaf plant height. The ground-measured plant height was set as the dependent variable (Y), and the independent variable (X) configurations used in each model were as follows.

1. Ground-based simple linear regression model (G-SLR): manually measured stem diameter.
2. UAV-based multiple linear regression model (UAV-MLR): mean values of vegetation indices (NDVI, GNDVI, GLI, NGBDI, NGRDI and VARI) and mean ΔDSM_t values extracted through object-based preprocessing.

The variance inflation factor (VIF) was used to diagnose multicollinearity among the independent variables in the initial UAV-MLR model, and variables with VIF > 10 were sequentially removed using backward elimination to determine the final linear model. The statistical adequacy of each final linear model was then evaluated through residual diagnostics. Homoscedasticity of the residuals was tested using the Breusch–Pagan test, and normality was assessed using the Shapiro–Wilk test.

Model fitting performance was evaluated on the calibration dataset using the coefficient of determination (R^2), adjusted coefficient of determination (adjusted R^2), root mean square error (RMSE), and mean absolute error (MAE). Considering the sample size of the dataset, all treatment means were used for calibration without separate training/validation partitioning or cross-validation. All statistical analyses were performed using R software (ver. 4.3.1) [54] with the "dplyr", "car", "lmtest", and "ggplot2" packages.

3. Results and Discussion

3.1. Growth Responses of Kenaf Under Fertilization Treatments

3.1.1. Temporal Variations in Plant Height

The time-series variation in kenaf plant height from 20 to 110 days after sowing (DAS) is presented in Table 3 and Figure 5a. The two-way ANOVA results showed that nitrogen fertilizer level and compost application had significant effects ($p < 0.05$) on plant height up to 80 DAS, but the effects were not significant at the harvest stage (110 DAS). During the vegetative growth stages at 20, 40, and 80 DAS, both nitrogen level and compost application significantly affected plant height, and their interaction was also significant ($p < 0.01$).

Table 3. Temporal variations in plant height of kenaf under different nitrogen levels and compost applications measured at different days after sowing (20 to 110 DAS).

Trait	Treatment	20 DAS	40 DAS	60 DAS †	80 DAS	110 DAS
Plant height (cm)	N0	33.9 ± 5.1 ^{c}	129.6 ± 3.5 ^{b}	206.2 ± 6.5	307.5 ± 5.1 ^{c}	376.2 ± 31.4
	N0+C	39.5 ± 4.8 ^{b}	123.2 ± 7.8 ^{b}	213.8 ± 4.7	319.1 ± 4.5 ^{c}	391.1 ± 22.6
	N0.5	32.3 ± 4.2 ^{c}	128.7 ± 3.5 ^{b}	208.8 ± 3.3	329.8 ± 4.5 ^{ab}	386.7 ± 14.9
	N0.5+C	50.5 ± 4.0 ^{a}	131.9 ± 11.0 ^{b}	209.6 ± 7.0	347.3 ± 8.9 ^{b}	424.5 ± 20.7
	N1	46.9 ± 3.4 ^{a}	139.1 ± 4.4 ^{a}	244.1 ± 9.2	323.1 ± 5.8 ^{b}	423.5 ± 7.3
	N1+C	47.9 ± 5.2 ^{a}	147.7 ± 6.3 ^{a}	256.9 ± 11.1	357.5 ± 7.4 ^{a}	432.4 ± 54.8
	N2	39.2 ± 2.3 ^{b}	135.6 ± 7.1 ^{ab}	227.7 ± 3.3	335.2 ± 8.3 ^{a}	429.8 ± 11.9
	N2+C	48.8 ± 1.4 ^{a}	157.8 ± 6.6 ^{a}	230.2 ± 3.2	340.5 ± 4.0 ^{b}	410.8 ± 38.3
Main Effects † (60 DAS)	Nitrogen	N0: 210.0 ^{c}	N0.5: 209.2 ^{c}	N1: 250.5 ^{a}	N2: 229.0 ^{b}	
	Compost	No compost: 221.7 ^{B}		Compost: 227.7 ^{A}		
Overall Effects	F-value (Two-way ANOVA)					
Nitrogen		12.48 ***	21.49 ***	51.79 ***	33.07 ***	2.68 ^{ns}

https://doi.org/10.3390/agronomy16181805

Compost	45.11 ***	10.54 **	4.85 *	59.35 ***	0.80 ns
Nitrogen × Compost	8.13 ***	7.98 ***	1.00 ns	7.83 ***	0.97 ns

Note: Values are presented as mean ± standard deviation (SD), rounded to the first decimal place. Treatment names indicate nitrogen fertilization rate and compost application. For 20, 40, and 80 DAS (where interaction effects were significant), different lowercase letters within a column indicate significant differences among Nitrogen levels within each individual Compost treatment group by Duncan's multiple range test ($p < 0.05$). † For 60 DAS (where the interaction effect was non-significant), the main effects of Nitrogen (lowercase letters) and Compost (uppercase letters) are independently presented at the bottom. Post hoc letters are omitted for 110 DAS due to the absence of significant variance in the two-way ANOVA. For overall effects, the values represent *F*-value from the two-way ANOVA. ns, *, **, and *** indicate non-significant and significant differences at $p < 0.05$, $p < 0.01$, and $p < 0.001$, respectively. Each treatment was conducted in triplicate (3 plots per treatment; total 24 plots), with each plot measuring 3 m × 3 m (9 m^2) at a 20 cm × 20 cm planting grid (~225 plants per plot, ~5400 plants across the 300 m^2 total field area). Plant height was measured by random ground sampling ($n = 5$ plants per treatment group at 20 and 40 DAS; $n = 3$ per treatment at 60 and 110 DAS; $n = 4$ per treatment at 80 DAS).

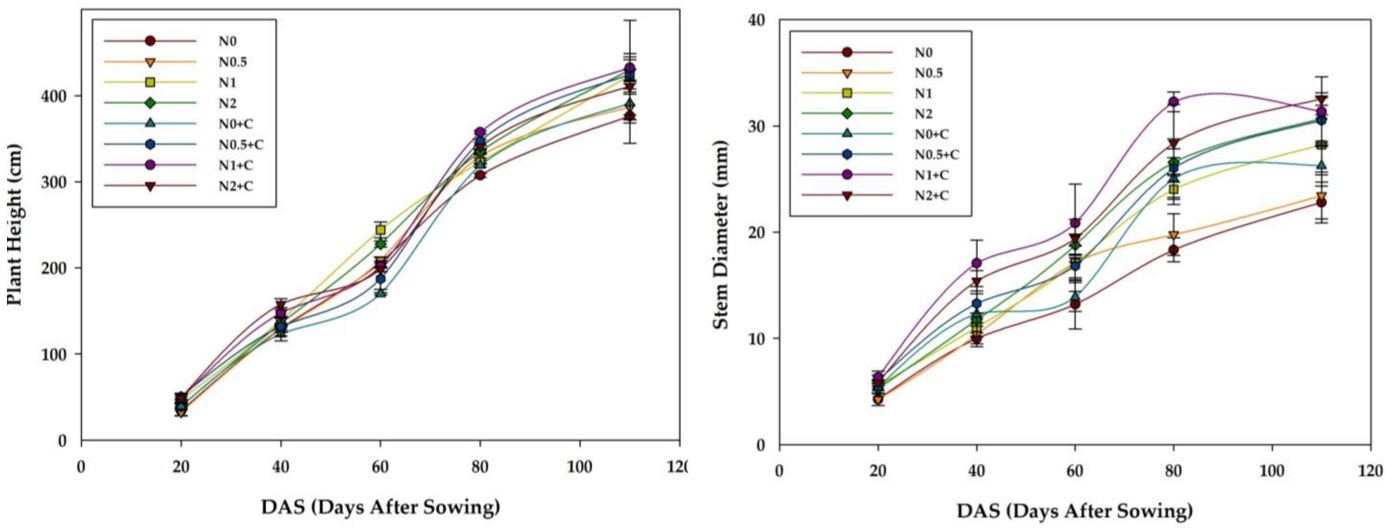

(**a**) (**b**)

Figure 5. Time-series growth curves of kenaf parameters under various nitrogen levels and compost applications measured throughout the growth period (20 to 110 DAS): (**a**) Sequential changes in plant height (cm) from 20 to 110 DAS. (**b**) Sequential changes in stem diameter (mm) from 20 to 110 DAS. The eight treatment lines correspond to N0, N0.5, N1, and N2 without compost, and N0+C, N0.5+C, N1+C, and N2+C with compost application. Vertical error bars represent the standard deviation ($n = 3$–5).

At the early growth stage (20 DAS), under the no-compost condition, the N1 treatment produced the greatest plant height (46.9 ± 3.4 cm). In contrast, N0.5+C treatment showed the highest value (50.5 ± 4.0 cm) under the compost application and did not differ significantly from the N1 and N2 treatments, suggesting that compost application may have buffered the growth response under reduced nitrogen supply. This trend continued at 40 DAS, where the N2+C treatment recorded the highest plant height (157.8 ± 6.6 cm) but was not significantly different from the N1+C treatment. These results suggest that the combined supply of organic and inorganic nutrients contributed to early vegetative growth promotion [55].

At 60 DAS, the interaction effect was not significant ($F = 1.00$, $p > 0.05$), so the main effects of each factor were examined separately. For nitrogen treatment, the N1 level showed the highest mean plant height at 250.5 cm regardless of compost application, followed by N2 (229.0 cm), N0 (210.0 cm), and N0.5 (209.2 cm). Compost application also had a significant effect ($F = 4.85$, $p < 0.05$), with the compost-applied plots (227.7 cm) showing greater plant height than the no-compost plots (221.7 cm). The disappearance of the interaction effect suggests that the difference between nitrogen levels became less dependent on compost status at this stage, possibly due to a temporary convergence in growth responses or environmental influences.

At 80 DAS, corresponding to the transition to the flowering stage, the interaction effect was significant again ($F = 7.83$, $p < 0.001$), indicating that treatment differences became more pronounced. Under the no-compost condition, N2 and N0.5 formed the upper group, whereas under compost application, N1+C showed the highest plant height at 357.5 ± 7.4 cm, supporting previous findings that the combined application of inorganic fertilizer and organic compost can optimize nutrient-use efficiency in kenaf during vegetative growth [16].

However, with the onset of the flowering stage after 80 DAS, a physiological shift became evident, and by the final harvest stage at 110 DAS, no significant treatment effects ($p > 0.05$) remained for nitrogen ($F = 2.68$), compost ($F = 0.80$), or their interaction ($F = 0.97$). This suggests that, after flowering initiation, metabolic energy and photosynthates were reallocated from vertical stem elongation during vegetative growth to the development of reproductive organs such as flowers and seeds [17,56].

As a result, the morphological differences formed by fertilization treatments during the vegetative growth stage tended to converge statistically by the final harvest stage. This suggests that, because plant height responsiveness to fertilization decreases after the onset of flowering, plant height may have limited value as an indicator for evaluating treatment effects during later growth stages [18,57,58].

3.1.2. Temporal Variations in Stem Diameter

The time-series variation in kenaf stem diameter is presented in Table 4 and Figure 5b. In contrast to plant height, whose significance disappeared after flowering, stem diameter was continuously and significantly affected by the main effects of nitrogen fertilizer level and compost application throughout the entire growth period up to the final harvest stage at 110 DAS ($p < 0.001$). This suggests that radial stem thickening continued to reflect the sustained allocation of assimilates later into development, rather than the vertical elongation observed in plant height [24,25,59].

Table 4. Temporal variations in stem diameter of kenaf under different nitrogen levels and compost applications measured at different days after sowing (20 to 110 DAS).

Trait	Treatment	20 DAS †	40 DAS	60 DAS †	80 DAS	110 DAS †
Stem diameter (mm)	N0	4.26 ± 0.60	9.98 ± 0.51 b	13.19 ± 2.33	18.34 ± 1.15 c	22.80 ± 1.93
	N0+C	5.40 ± 0.58	12.29 ± 2.17 b	15.29 ± 0.87	25.07 ± 1.96 c	26.25 ± 1.92
	N0.5	4.23 ± 0.56	10.34 ± 1.13 b	17.11 ± 2.70	19.78 ± 1.96 ab	23.45 ± 2.20
	N0.5+C	6.04 ± 0.51	13.28 ± 0.89 b	19.11 ± 0.95	26.04 ± 2.75 b	30.52 ± 2.14
	N1	5.54 ± 0.49	11.04 ± 0.86 a	17.07 ± 1.64	24.04 ± 1.43 b	28.22 ± 2.83
	N1+C	6.32 ± 0.59	17.08 ± 2.19 a	21.77 ± 1.13	32.26 ± 0.92 a	31.36 ± 3.29
	N2	5.27 ± 0.50	11.73 ± 0.59 ab	18.79 ± 0.99	26.58 ± 1.25 a	30.69 ± 2.12
	N2+C	5.80 ± 0.31	15.40 ± 0.98 a	22.46 ± 1.19	28.39 ± 3.66 b	32.53 ± 0.61
Main Effects †	Nitrogen	N0: 4.83 c		N0: 14.24 c		N0: 24.53 b
		N0.5: 5.13 bc		N0.5: 18.11 b		N0.5: 26.99 b
		N1: 5.93 a		N1: 19.42 ab		N1: 29.79 a
		N2: 5.54 ab		N2: 20.63 a		N2: 31.61 a

	Compost	No compost: 4.82 [B] Compost: 5.89 [A]		No compost: 16.54 [B] Compost: 19.66 [A]		No compost: 26.29 [B] Compost: 30.17 [A]
Overall effects	F-value (Two-way ANOVA)					
Nitrogen		8.35 ***	11.18 ***	17.77 ***	19.42 ***	11.48 ***
Compost		41.32 ***	80.49 ***	22.57 ***	61.66 ***	17.79 ***
Nitrogen × Compost		2.77 [ns]	3.82 *	0.99 [ns]	3.55 *	1.49 [ns]

Note: Values are presented as mean ± standard deviation (SD), rounded to the second decimal place. Treatment names indicate nitrogen fertilization rate and compost application. For 40 and 80 DAS, where interaction effects were significant, different lowercase letters within each compost condition indicate significant differences among nitrogen levels according to Duncan's multiple range test (p < 0.05). [†] For 20, 60, and 110 DAS, where interaction effects were non-significant, the main effects of nitrogen (lowercase letters) and compost (uppercase letters) are independently presented at the bottom. For overall effects, the values represent F-value from the two-way ANOVA. [ns], *, and *** indicate non-significant and significant differences at $p < 0.05$, $p < 0.01$, and $p < 0.001$, respectively. Each treatment was conducted in triplicate (3 plots per treatment; total 24 plots), with each plot measuring 3 m × 3 m (9 m^2) at a 20 cm × 20 cm planting grid (~225 plants per plot, ~5400 plants across the 300 m^2 total field area). Stem diameter was measured by random ground sampling (n = 5 plants per treatment group at 20 and 40 DAS; n = 3 per treatment at 60 and 110 DAS; n = 4 per treatment at 80 DAS).

The nitrogen × compost interaction effect (N × C) was significant at 40 DAS ($F = 3.82$, $p < 0.05$) and 80 DAS ($F = 3.55$, $p < 0.05$), when growth was most vigorous. At 40 DAS, under compost application, the effect of nitrogen treatment was clearly expressed, with the N1 treatment showing the highest value at 17.08 ± 2.19 mm, and the N2 treatment also belonging to the upper group. In contrast, under the no-compost condition, no consistent increase in stem diameter was observed with increasing nitrogen level. At 80 DAS, under no-compost conditions, N2 formed the upper group, whereas under compost application, N1 showed the highest stem diameter at 32.26 ± 0.92 mm. These results indicate that nitrogen fertilization effects were differently expressed depending on compost application, suggesting that the combined use of organic and inorganic nutrients may act in a complementary manner to promote stem thickening growth [60,61].

At 20, 60, and 110 DAS, the interaction effect was not significant, so the results were interpreted mainly in terms of the main effects. At the early growth stage (20 DAS), among the nitrogen treatments, N1 showed the highest mean value at 5.93 mm, and the compost-applied plots (5.89 mm) were significantly higher than the no-compost plots (4.82 mm). At 60 DAS, N2 formed the highest group (a), while N1 was placed in the intermediate group (ab), followed by N0.5 and N0. Compost application also showed a significant effect, with the applied plots (19.66 mm) exhibiting higher values than the no-compost plots (16.54 mm).

At 110 DAS, stem thickening continued even after flowering, and the main effects of nitrogen and compost remained significant ($p < 0.001$). Under nitrogen treatment, N2 (31.61 mm) and N1 (29.79 mm) formed the upper group, while the compost-applied plots showed a significantly higher mean stem diameter (30.17 mm) than the no-compost plots (26.29 mm). The observed increases in stem diameter under nitrogen fertilization and compost application suggest that, after flowering, assimilates not used for longitudinal growth were redistributed to the development of structural stem tissues such as xylem and bast fibers [62,63].

This sustained responsiveness in stem diameter is considered an important physiological mechanism in bast fiber crops such as kenaf, as it can enhance structural stability, suppress lodging, and help secure final fiber biomass productivity [64,65].

3.2. UAV-Based Vegetation Indices and Digital Surface Model Analysis

3.2.1. Vegetation Indices Analysis

The temporal variation patterns of six vegetation indices derived from UAV remote sensing at each growth stage are presented in Figure 6. NDVI (Figure 6a) and GNDVI (Figure 6b), both of which include the near-infrared (NIR) band, increased rapidly from the early growth stage (20 DAS) to the 40–60 DAS period and then remained stably high throughout the remainder of the growth period. In particular, the N0 and N0+C treatments maintained relatively low values throughout the entire period, whereas the nitrogen-fertilized treatments (N1 and N2) were mainly distributed within the higher value range. This suggests that NIR-based vegetation indices respond sensitively to kenaf biomass accumulation and changes in chlorophyll activity, making them useful for long-term tracking of nitrogen fertilization effects [66,67].

In contrast, the visible-band indices GLI (Figure 6c), NGBDI (Figure 6d), and NGRDI (Figure 6e) reached their maximum values at 40–60 DAS and then tended to decrease at 80 DAS. This pattern could potentially be explained by canopy closure alongside possible later-stage declines in chlorophyll content and leaf color changes [68,69]. In addition, increased shading caused by greater canopy density and changes in visible-band reflectance properties likely contributed to the reduced sensitivity of these indices [70]. By 110 DAS, a slight increase was observed in some indices, which may be explained by greater structural heterogeneity and increased exposure of lower vegetation layers in the late growth stage [71].

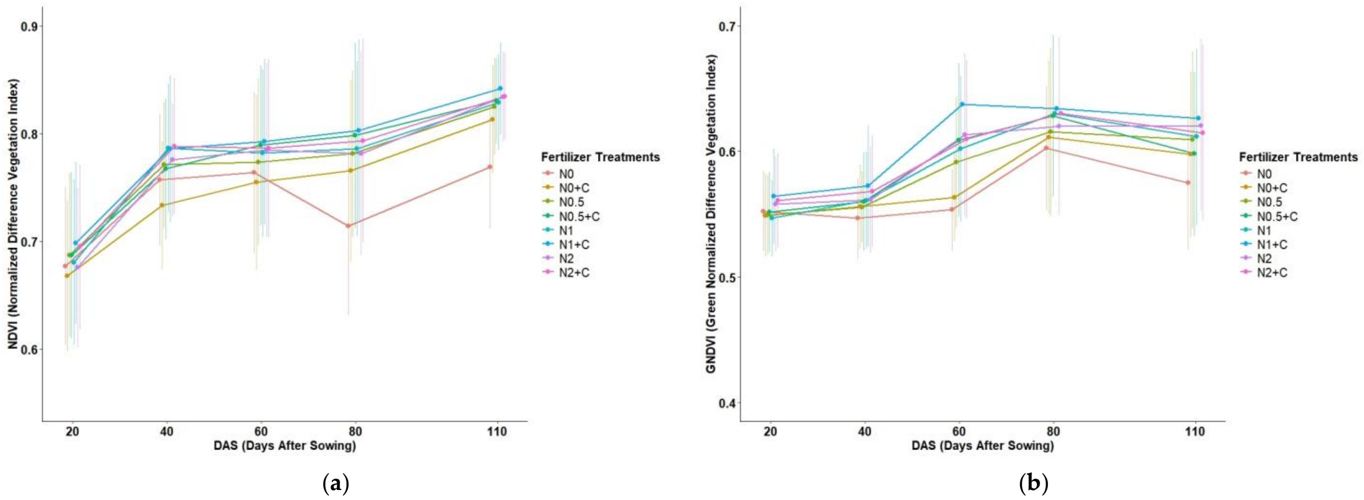

(**a**) (**b**)

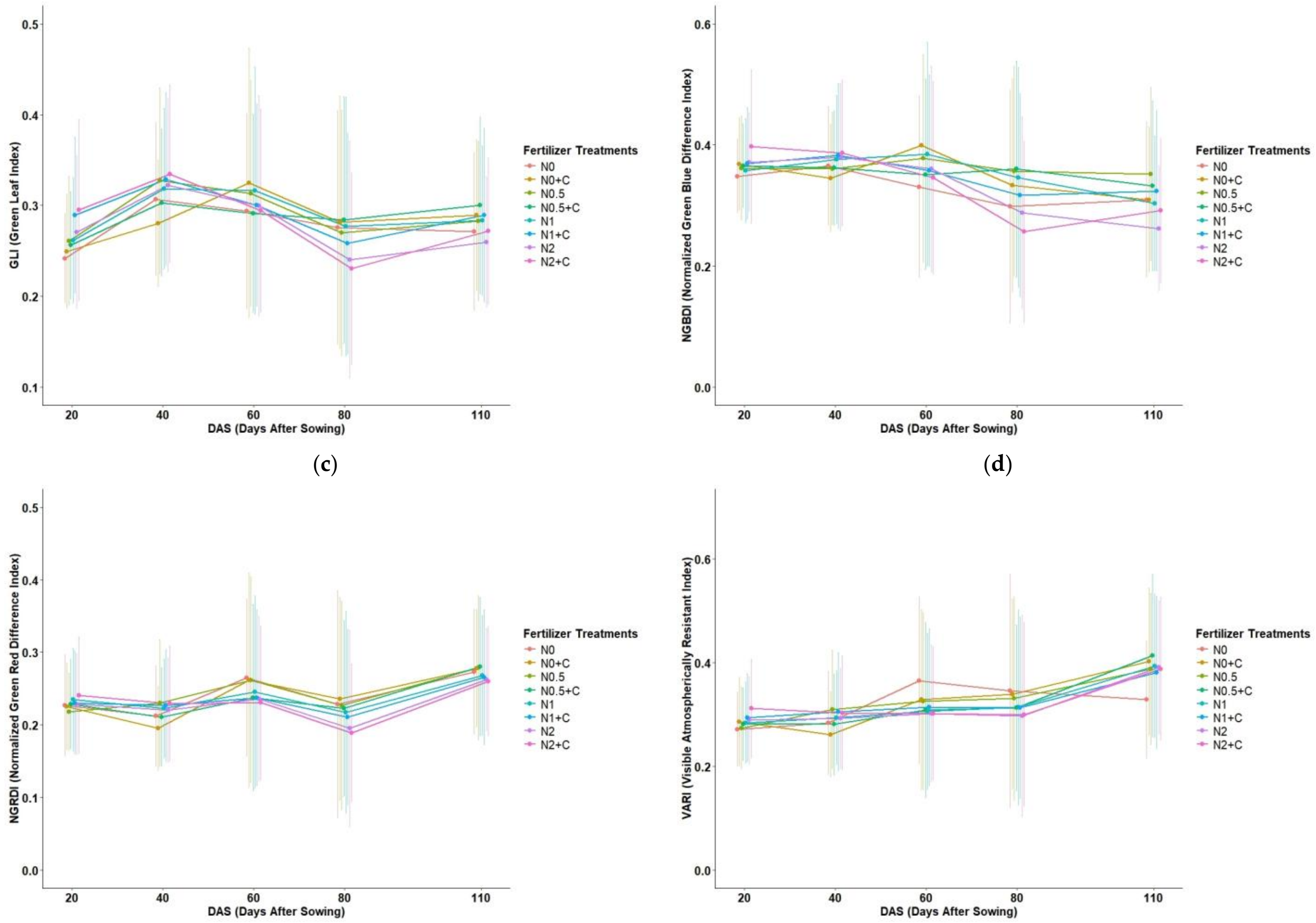

(**c**) (**d**)

(**e**) (**f**)

Figure 6. Time-series changes in UAV-based vegetation indices under different nitrogen and compost treatments during the kenaf growth period: (**a**) NDVI; (**b**) GNDVI; (**c**) GLI; (**d**) NGBDI; (**e**) NGRDI; (**f**) VARI. Vertical error bars represent the standard deviation of the region of interest (ROI) for each treatment.

VARI (Figure 6f), unlike the other visible-band indices, showed a distinct temporal pattern with a gradual increase continuing into the late growth stage (110 DAS). This is likely because VARI is relatively less sensitive to atmospheric effects and soil background influences, and therefore more stably reflects green reflectance characteristics within the canopy [43].

In this study, NDVI and GNDVI showed high sensitivity in reflecting biomass accumulation and nitrogen responsiveness, whereas the visible-band indices provided useful information for capturing structural and physiological transitions at specific growth stages. The differing response characteristics among these indices may help promote complementarity among predictors, and thus they could serve as an important set of independent variables for improving the explanatory power of future multiple regression and machine learning-based prediction models.

3.2.2. Canopy Structure Development Based on Relative Digital Surface Model (ΔDSM_t)

Using UAV-based digital surface model analysis (ΔDSM_t), the vertical structural development of the kenaf canopy at each growth stage was tracked, and the canopy development and spatial patterns varied depending on the fertilizer level and compost application (Figure 7).

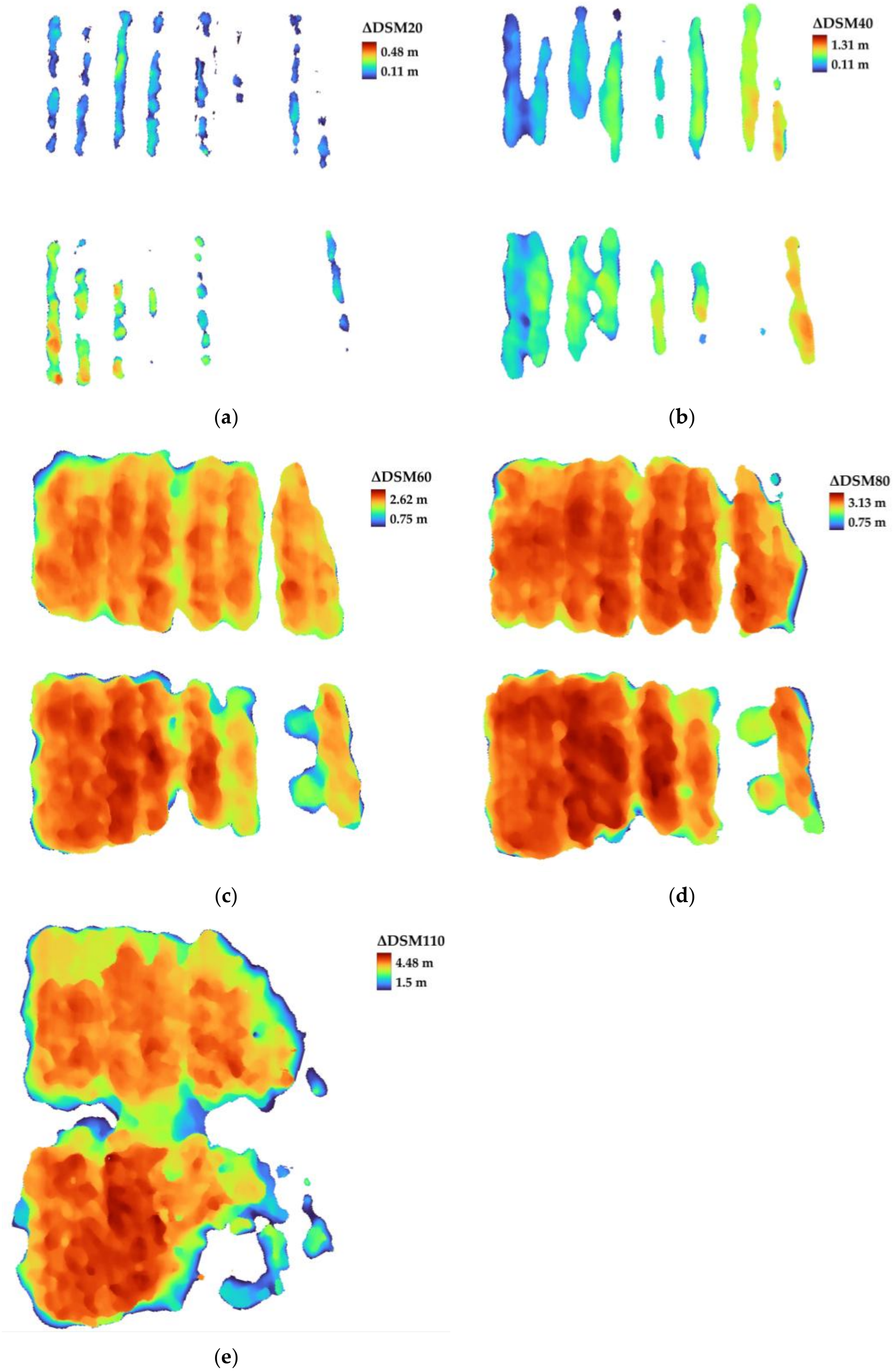

Figure 7. Spatio-temporal progression of the relative digital surface model (ΔDSM_t) across different growth stages: (**a**) 20 DAS; (**b**) 40 DAS; (**c**) 60 DAS; (**d**) 80 DAS; (**e**) 110 DAS. The color scale illustrates variations in pure vegetation height, reflecting the differential growth responses to fertilization treatments.

At the early growth stage, from 20 DAS to the vegetative transition period at 40 DAS, individual vegetation pixels tended to remain separately partitioned along the sowing rows, while canopy expansion across treatments progressed gradually (Figure 7a,b).

However, by the middle vegetative stage (60–80 DAS), neighboring canopies increasingly merged, and the entire field began to form a continuous canopy layer (Figure 7c,d).

During this period, red-colored areas indicating greater relative canopy height were more developed in the treatments with higher nitrogen rates and compost application, whereas blue and green areas, which represent limited vertical growth, remained in the nutrient-deficient treatments, highlighting clear spatial variation among treatments. These results suggest that fertilization conditions influenced the vertical structural development of the kenaf canopy [45].

At the harvest stage (110 DAS), the final vertical structure of the canopy appeared to have been established, and the persistent height differences across the canopy and along treatment boundaries suggest that fertilization conditions may have influenced the final stand structure of the kenaf crop (Figure 7e).

In this study, the vertical growth model constructed using ΔDSM_t showed some deviation when compared with the plant height measured directly in the field. This discrepancy between UAV-based height estimates and ground-measured plant height is a typical feature of canopy-based remote sensing analysis. Ground-measured plant height is calculated as the vertical distance to the tip of the uppermost apical leaf, whereas DSM reflects the average height of the upper canopy surface at the pixel level, which tends to result in slight structural underestimation [41,72].

Moreover, as the growth stage progressed, the kenaf canopy became denser, reducing light penetration into the interior of the canopy. In particular, the irregular canopy structure observed in the nitrogen-deficient plots may have increased subtle shadows and ground noise within pixels, making it difficult to rule out the possibility that errors were introduced during the alignment process [73].

Nevertheless, the time-series upward trend observed in ΔDSM_t and the relative growth differences among treatments showed a pattern broadly similar to the actual plant height development and the trends in the vegetation indices described above, such as NDVI. In conclusion, the ΔDSM_t visualization in this study can serve as a useful auxiliary tool for non-destructively evaluating spatial growth differences across the field and the dynamics of vertical structural development at the canopy level when used together with individual plant height measurements.

3.3. UAV-Based Canopy Height Prediction Model Development and Comparative Analysis

3.3.1. Variable Selection and UAV-MLR Model Development Based on Multicollinearity Control

To non-destructively estimate kenaf plant height using UAV remote sensing data, ΔDSM_t, a processed digital surface model variable, and the mean values of six vegetation indices (NDVI, GNDVI, GLI, NGBDI, NGRDI, and VARI) were initially set as candidate independent variables. Because some vegetation indices derived from multispectral and RGB imagery share overlapping spectral information, they can induce multicollinearity in the model. To control this, multicollinearity was assessed using the variance inflation factor (VIF), and variables with VIF values exceeding 10 were sequentially removed using a backward elimination approach.

GLI, NGBDI, and VARI were excluded from the initial model because they showed high multicollinearity or relatively low contributions. In the final model, VIF values for all independent variables (ΔDSM_t, NDVI, GNDVI, NGRDI) ranged from 1.19 to 6.35, indicating that multicollinearity was reduced to below the commonly used threshold of 10.

To minimize distortion in regression coefficients caused by differences in variable scale, each independent variable was standardized before constructing the multiple linear regression (MLR) model. The final UAV-based multiple linear regression model is presented in Equation (4).

https://doi.org/10.3390/agronomy16181805

$$\text{Predicted Plant Height (cm)} = 229.13 + 121.58 \times \text{scale}(\Delta DSM_t) + 34.15 \times \text{scale(NDVI)} - 14.30 \times \text{scale(GNDVI)} - 8.45 \times \text{scale(NGRDI)} \quad (4)$$

This model was interpreted as the combination of a vertical structural variable (ΔDSM_t) and spectral vegetation indices (NDVI, GNDVI, and NGRDI) that reflect canopy structure and vigor, thereby compensating for the limitations of a single remote sensing variable in explanatory power [44].

3.3.2. Performance Comparison and Suitability Assessment with G-SLR

The predictive performance and goodness of fit of the ground-based simple linear regression model (G-SLR), constructed from data directly measured in the field using a measuring tape and digital calipers, and the UAV-based multiple linear regression model (UAV-MLR), built using UAV-processed data, were compared and analyzed (Table 5). The G-SLR model was developed after applying natural logarithmic transformation to both variables to account for the nonlinear relationship between stem diameter and plant height.

Table 5. Comparison of kenaf plant height fitting performance between the Ground-based simple linear regression model (G-SLR) and the UAV-based multiple linear regression model (UAV-MLR).

Indicator	Model Type	
	G-SLR	**UAV-MLR**
Predictor Variables	ln(Stem Diameter)	Standardized ΔDSM_t, NDVI, GNDVI, NGRDI
R^2	0.9625	0.9873
Adjusted R^2	0.9615	0.9858
RMSE	39.68	14.95
MAE	29.16	11.31
Normality (p-value)	0.1773	0.6709
Heteroscedasticity (p-value)	0.5113	0.3392

Abbreviations: R^2—coefficient of determination; RMSE—root mean squared error; MAE—mean absolute error.

In the comparative analysis, the adjusted R^2 of the G-SLR model was 0.9615, indicating a strong positive linear relationship, and the residuals satisfied the assumptions of normality (Shapiro–Wilk, $p = 0.1773$) and homoscedasticity (Breusch–Pagan, $p = 0.5113$). However, when RMSE and MAE were calculated based on predictions back-transformed to the original cm scale using the exponential function, the values were 39.68 cm and 29.16 cm, respectively. This may be because the developmental patterns of stem thickening and vertical elongation did not fully coincide during the later growth stage [20,26].

On the other hand, the UAV-MLR model showed high explanatory power, with an adjusted R^2 of 0.9858 and an F-statistic of 678.4 ($p < 0.001$), while also yielding lower errors than the G-SLR model, with an RMSE of 14.95 cm and an MAE of 11.31 cm. Residual diagnostics further confirmed that both normality (Shapiro–Wilk, $p = 0.6709$) and homoscedasticity (Breusch–Pagan, $p = 0.3392$) were satisfied, indicating that the regression assumptions were met. Accordingly, the UAV-MLR was considered a more accurate and suitable non-destructive estimation model for predicting kenaf plant height than the ground-based G-SLR.

3.3.3. Discussion of Remote Sensing Model and Implications for Precision Agriculture

The UAV-based multiple linear regression model developed in this study showed strong fitting performance for kenaf plant height, which can be interpreted as the result of the complementary roles of ΔDSM_t, reflecting vertical structure, and vegetation indices, reflecting the physiological status of the canopy. In other words, height variation that is difficult to capture with a single remote sensing variable could be explained more precisely by combining vertical and spectral information. These findings suggest that a UAV-based multivariate approach can be an effective methodology for quantifying the growth characteristics of tall crops [74,75].

It is worth noting that ΔDSM_t in this study was explicitly derived relative to the bare soil baseline ($DSM_t - DSM_{pre}$) to enable instantaneous estimation of absolute plant height from a single UAV flight. Incorporating prior height (H_{t-1}) or interval height differences ($DSM_t - DSM_{t-1}$) would shift the modeling framework from absolute status mapping to dynamic incremental growth forecasting. Although such autoregressive growth modeling represents a different conceptual framework from our single-flight mapping objective, integrating sequential height baselines offers a promising avenue for future multi-temporal studies to mitigate spectral saturation during dense canopy stages.

In crops such as kenaf, which continue vertical growth until the later growth stages and show spatial heterogeneity in treatment responses, conventional ground surveys alone are often insufficient to fully capture field variability. In contrast, UAV remote sensing enables repeated observations over the entire plot area, making it possible to obtain field-scale canopy information rather than measurements limited to individual plants. Therefore, unlike direct measurements at the plant level, the approach used in this study is useful for precise growth assessment because it can also account for the spatial distribution of growth across the field [76].

Moreover, this study suggests that the UAV-based model can improve not only the accuracy of plant height prediction but also its practical value for precision agriculture. For example, UAV-derived data can provide objective information while reducing labor and time requirements for tasks such as monitoring fertilizer responses by growth stage, tracking canopy development, and comparing treatment effects [77]. Under large-scale cultivation or when field access is limited, this non-destructive assessment method may be even more useful [78]. Therefore, the UAV-based plant height prediction model proposed in this study can serve as a practical reference for large-scale growth diagnosis and efficient field management strategies for kenaf, a tall forage crop.

4. Conclusions

This study evaluated the growth characteristics of kenaf and the feasibility of non-destructive plant height estimation by comparing the time-series responses of plant height and stem diameter to fertilization treatments, as well as the performance of UAV-based prediction models. Plant height was strongly influenced by nitrogen fertilization and compost application from the early to mid-growth stages, but the differences among treatments gradually decreased as the crop entered the reproductive growth stage. In contrast, stem diameter maintained a persistent fertilization response until the late growth stage, indicating that it more stably reflected long-term nutrient responsiveness than plant height.

The UAV-based multiple linear regression model (UAV-MLR), using ΔDSM_t and vegetation indices (NDVI, GNDVI, and NGRDI), showed high explanatory power and low fitting error and outperformed the ground-based simple linear regression model (G-SLR) in estimating kenaf plant height. This indicates that UAV data are effective for non-destructive and accurate estimation of kenaf plant height by simultaneously reflecting both the vertical structure and physiological vigor of the canopy.

https://doi.org/10.3390/agronomy16181805

In conclusion, this study confirmed the practical potential of UAV-based remote sensing to complement conventional ground surveys for tall crops such as kenaf. Although no direct chemical analysis of plant internal components was conducted, the non-destructive growth information framework proposed in this study can serve as a useful basis for large-scale crop monitoring and fertilization management in precision agriculture. Future work should further validate the model across multiple cultivars, growth stages, and environmental conditions to improve its generalizability.:

Author Contributions: Conceptualization—T.Y., T.K. and S.Y.; methodology—T.Y.; validation—T.Y., T.K. and S.Y.; formal analysis—T.Y.; investigation—T.Y.; resources—T.Y.; data curation—T.Y.; writing—original draft preparation—T.Y.; writing—review and editing—T.Y., T.K. and S.Y.; visualization—T.Y.; supervision—T.K. and S.Y.; project administration—T.Y. All authors have read and agreed to the published version of the manuscript.

Funding: This study was supported by the Korea Institute of Planning and Evaluation for Technology in Food, Agriculture and Forestry (IPET) through the Agriculture and Food Convergence Technologies Program for Research Manpower development, funded by the Ministry of Agriculture, Food and Rural Affairs (MAFRA) (RS-2024-00400922).

Data Availability Statement: The original contributions presented in this study are included in the article. Further inquiries can be directed to the corresponding authors.

Acknowledgments: We thank the editors and reviewers for their time and expertise. Their thoughtful evaluations and suggestions contributed considerably to refining the manuscript and strengthening the scientific contribution of this work.

Conflicts of Interest: The authors declare no conflicts of interest.

Abbreviations

The following abbreviations are used in this manuscript:

DAS	Days after sowing
UAV	Unmanned aerial vehicle
DSM	Digital surface model
DSM_t	Relative digital surface model at time t
DSM_{pre}	Digital surface model before sowing
NDVI	Normalized difference vegetation index
GNDVI	Green normalized difference vegetation index
GLI	Green leaf index
NGBDI	Normalized green blue difference index
NGRDI	Normalized green red difference index
VARI	Visible atmospherically resistant index
MLR	Multiple linear regression
G-SLR	Ground-based simple linear regression
UAV-MLR	UAV-based multiple linear regression
VIF	Variance inflation factor
RMSE	Root mean square error
MAE	Mean absolute error
R^2	Coefficient of determination
Adj. R^2	Adjusted coefficient of determination

References

1. Agreement, P. Paris agreement. In Proceedings of the Report of the Conference of the Parties to the United Nations Framework Convention on Climate Change (21st Session, 2015: Paris), Paris, France, 30 November–13 December 2015; p. 2.
2. Masson-Delmotte, V. *Global Warming of 1.5 °C: An IPCC Special Report on the Impacts of Global Warming of 1.5 °C Above Pre-Industrial Levels and Related Global Greenhouse Gas Emission Pathways, in the Context of Strengthening the Global Response to the Threat of Climate Change, Sustainable Development, and Efforts to Eradicate Poverty*; World Meteorological Organization: Geneva, Switzerland, 2018.
3. Office for Government Policy Coordination. *2050 Carbon Neutrality Scenario*; Joint Ministries: Sejong, Republic of Korea, 2021.
4. Balafoutis, A.; Beck, B.; Fountas, S.; Vangeyte, J.; Van der Wal, T.; Soto, I.; Gómez-Barbero, M.; Barnes, A.; Eory, V. Precision agriculture technologies positively contributing to GHG emissions mitigation, farm productivity and economics. *Sustainability* **2017**, *9*, 1339. https://doi.org/10.3390/su9081339.
5. Getahun, S.; Kefale, H.; Gelaye, Y. Application of precision agriculture technologies for sustainable crop production and environmental sustainability: A systematic review. *Sci. World J.* **2024**, *2024*, 2126734. https://doi.org/10.1155/2024/2126734.
6. Petrovic, B.; Csambalik, L. Enhancing precision agriculture for climate change mitigation in Visegrad countries: Factors shaping adaptation. *Land* **2025**, *14*, 399. https://doi.org/10.3390/land14020399.
7. Alexopoulou, E.; Christou, M.; Mardikis, M.; Chatziathanassiou, A. Growth and yields of kenaf varieties in central Greece. *Ind. Crops Prod.* **2000**, *11*, 163–172. https://doi.org/10.1016/S0926-6690(99)00064-3.
8. Danalatos, N.; Archontoulis, S. Growth and biomass productivity of kenaf (*Hibiscus cannabinus* L.) under different agricultural inputs and management practices in central Greece. *Ind. Crops Prod.* **2010**, *32*, 231–240. https://doi.org/10.1016/j.indcrop.2010.04.013.
9. Lam, T.B.T.; Hori, K.; Iiyama, K. Structural characteristics of cell walls of kenaf (*Hibiscus cannabinus* L.) and fixation of carbon dioxide. *J. Wood Sci.* **2003**, *49*, 255–261. https://doi.org/10.1007/s10086-002-0469-7.
10. Li, D.; Huang, S. The breeding of kenaf. In *Kenaf: A Multi-Purpose Crop for Several Industrial Applications: New Insights from the Biokenaf Project*; Springer: Berlin/Heidelberg, Germany, 2013; pp. 45–58. https://doi.org/10.1007/978-1-4471-5067-1_3.
11. Alexopoulou, E.; Papatheohari, Y.; Christou, M.; Monti, A. Origin, description, importance, and cultivation area of kenaf. In Kenaf: a multi-purpose crop for several industrial applications: new insights from the Biokenaf project; Springer: Berlin/Heidelberg, Germany, 2013; pp. 1-15. https://doi.org/10.1007/978-1-4471-5067-1_1.
12. Kim, J.; Han, G.D.; Muthukathan, G.; Rodrogues, R.; Hyun, D.Y.; Kim, S.-H.; Yu, J.-K.; Park, J.; Yoo, S.-C.; Chung, Y.S. What Traits Should Be Measured for Biomass in Kenaf? *Plants* **2021**, *10*, 1394. https://doi.org/10.3390/plants10071394.
13. Fernando, A. Environmental aspects of kenaf production and use. In *Kenaf: A Multi-Purpose Crop for Several Industrial Applications: New Insights from the Biokenaf Project*; Springer: Berlin/Heidelberg, Germany, 2013; pp. 83–104. https://doi.org/10.1007/978-1-4471-5067-1_5.
14. Junejo, N.; Abdu, A.; Hamid, H.A.; Ahmed, K.; Akber, M.H. Journey of kenaf in Malaysia: A Review. *Sci. Res. Essays* **2014**, *9*, 458–470. https://doi.org/10.5897/SRE12.471.
15. Zhu, Z.; An, X.; Chen, C.; Luo, X.; Liu, T.; Zou, L.; Li, S. Effect of different fertilization strategies on phenotypic traits, yield and fiber quality of kenaf (*Hibiscus cannabinus* L.). *J. Nat. Fibers* **2025**, *22*, 2462978. https://doi.org/10.1080/15440478.2025.2462978.
16. OOlanipekun, S.; OTogun, A.; KAdebayo, A.; BAnjorin, F. Effects of organic and inorganic fertilizers on the growth and yield of kenaf (*Hibiscus cannabinus* L.) production in South Western Nigeria. *Int. J. Plant Soil Sci.* **2021**, *33*, 1–9. https://doi.org/10.9734/IJPSS/2021/v33i230408.
17. Shukor, N.A.A.; Hamzah, M.B.; Hamid, H.A.; Salleh, G.; Nasir, M.F.M. Growth and phenology of kenaf (*Hibiscus cannabinus* L.) varieties. *Pertanika J. Trop. Agric. Sci.* **2009**, *32*, 29–33.
18. Patanè, C.; Cosentino, S.L. Yield, water use and radiation use efficiencies of kenaf (*Hibiscus cannabinus* L.) under reduced water and nitrogen soil availability in a semi-arid Mediterranean area. *Eur. J. Agron.* **2013**, *46*, 53–62. https://doi.org/10.1016/j.eja.2012.12.002.
19. Bendig, J.; Bolten, A.; Bareth, G. UAV-based imaging for multi-temporal, very high resolution crop surface models to monitor crop growth variability. *Photogramm.-Fernerkund.-Geoinf.* **2013**, *2013*, 551–562. https://doi.org/10.1127/1432-8364/2013/0200.
20. Varela, S.; Assefa, Y.; Vara Prasad, P.; Peralta, N.R.; Griffin, T.W.; Sharda, A.; Ferguson, A.; Ciampitti, I.A. Spatio-temporal evaluation of plant height in corn via unmanned aerial systems. *J. Appl. Remote Sens.* **2017**, *11*, 036013. https://doi.org/10.1117/1.JRS.11.036013.
21. Araus, J.L.; Cairns, J.E. Field high-throughput phenotyping: The new crop breeding frontier. *Trends Plant Sci.* **2014**, *19*, 52–61. https://doi.org/10.1016/j.tplants.2013.09.008.

22. Ji, Y.; Chen, Z.; Cheng, Q.; Liu, R.; Li, M.; Yan, X.; Li, G.; Wang, D.; Fu, L.; Ma, Y. Estimation of plant height and yield based on UAV imagery in faba bean (*Vicia faba* L.). *Plant Methods* **2022**, *18*, 26. https://doi.org/10.1186/s13007-022-00861-7.
23. Yuan, H.; Song, M.; Liu, Y.; Xie, Q.; Cao, W.; Zhu, Y.; Ni, J. Field phenotyping monitoring systems for high-throughput: A survey of enabling technologies, equipment, and research challenges. *Agronomy* **2023**, *13*, 2832. https://doi.org/10.3390/agronomy13112832.
24. Marcelis, L. Sink strength as a determinant of dry matter partitioning in the whole plant. *J. Exp. Bot.* **1996**, *47*, 1281–1291.
25. Hossain, M.; Hanafi, M.; Saleh, G.; Foroughi, M.; Behmaram, R.; Noori, Z. Growth, photosynthesis and biomass allocation of different kenaf (*Hibiscus cannabinus* L.) accessions grown on sandy soil. *Aust. J. Crop Sci.* **2012**, *6*, 480–487.
26. Thornley, J.H. Modelling stem height and diameter growth in plants. *Ann. Bot.* **1999**, *84*, 195–205. https://doi.org/10.1006/anbo.1999.0908.
27. Zhang, C.; Kovacs, J.M. The application of small unmanned aerial systems for precision agriculture: A review. *Precis. Agric.* **2012**, *13*, 693–712. https://doi.org/10.1007/s11119-012-9274-5.
28. Tsouros, D.C.; Bibi, S.; Sarigiannidis, P.G. A review on UAV-based applications for precision agriculture. *Information* **2019**, *10*, 349. https://doi.org/10.3390/info10110349.
29. Phang, S.K.; Chiang, T.H.A.; Happonen, A.; Chang, M.M.L. From satellite to UAV-based remote sensing: A review on precision agriculture. *IEEE Access* **2023**, *11*, 127057–127076. https://doi.org/10.1109/ACCESS.2023.3330886.
30. Eves, A.; Stewart, T.P.; Gay, A.P.; Kemp, A.; Easey, M.; Angel, R.; Thomas, N.; Pearce, D. Developing unmanned aerial vehicles for local and flexible environmental and agricultural monitoring. In Proceedings of the New Dimensions in Earth Observation. Remote Sensing and Photogrammetry Society Conference, Leicester, UK, 8–11 December 2009.
31. Lee, K.; Lee, Y.-E.; Park, C.-W.; Hong, S.-Y.; Na, S. Study on reflectance and NDVI of aerial images using a fixed-wing UAV "Ebee". *Korean J. Soil Sci. Fert.* **2016**, *49*, 731–742. https://doi.org/10.7745/KJSSF.2016.49.6.731.
32. Murugan, D.; Garg, A.; Singh, D. Development of an adaptive approach for precision agriculture monitoring with drone and satellite data. *IEEE J. Sel. Top. Appl. Earth Obs. Remote Sens.* **2017**, *10*, 5322–5328. https://doi.org/10.1109/JSTARS.2017.2746185.
33. Mancini, A.; Frontoni, E.; Zingaretti, P. Satellite and uav data for precision agriculture applications. In Proceedings of the 2019 International Conference on Unmanned Aircraft Systems (ICUAS), Atlanta, GA, USA, 11–14 June 2019; pp. 491–497. https://doi.org/10.1109/ICUAS.2019.8797930.
34. Yu, D.; Zha, Y.; Shi, L.; Jin, X.; Hu, S.; Yang, Q.; Huang, K.; Zeng, W. Improvement of sugarcane yield estimation by assimilating UAV-derived plant height observations. *Eur. J. Agron.* **2020**, *121*, 126159. https://doi.org/10.1016/j.eja.2020.126159.
35. Yoon, T.; Kim, T.; Yoo, S. Non-Destructive Drone-Based Multispectral and RGB Image Analyses for Regression Modeling to Assess Waterlogging Stress in *Pseudolysimachion linariifolium*. *Horticulturae* **2025**, *11*, 1139. https://doi.org/10.3390/horticulturae11091139.
36. Chang, A.; Jung, J.; Maeda, M.M.; Landivar, J. Crop height monitoring with digital imagery from Unmanned Aerial System (UAS). *Comput. Electron. Agric.* **2017**, *141*, 232–237. https://doi.org/10.1016/j.compag.2017.07.008.
37. Oehme, L.H.; Reineke, A.-J.; Weiß, T.M.; Würschum, T.; He, X.; Müller, J. Remote sensing of maize plant height at different growth stages using UAV-based digital surface models (DSM). *Agronomy* **2022**, *12*, 958. https://doi.org/10.3390/agronomy12040958.
38. Ten Harkel, J.; Bartholomeus, H.; Kooistra, L. Biomass and crop height estimation of different crops using UAV-based LiDAR. *Remote Sens.* **2019**, *12*, 17. https://doi.org/10.3390/rs12010017.
39. Bendig, J.; Bolten, A.; Bennertz, S.; Broscheit, J.; Eichfuss, S.; Bareth, G. Estimating biomass of barley using crop surface models (CSMs) derived from UAV-based RGB imaging. *Remote Sens.* **2014**, *6*, 10395–10412. https://doi.org/10.3390/rs61110395.
40. Xie, T.; Li, J.; Yang, C.; Jiang, Z.; Chen, Y.; Guo, L.; Zhang, J. Crop height estimation based on UAV images: Methods, errors, and strategies. *Comput. Electron. Agric.* **2021**, *185*, 106155. https://doi.org/10.1016/j.compag.2021.106155.
41. Han, X.; Thomasson, J.A.; Bagnall, G.C.; Pugh, N.A.; Horne, D.W.; Rooney, W.L.; Jung, J.; Chang, A.; Malambo, L.; Popescu, S.C. Measurement and calibration of plant-height from fixed-wing UAV images. *Sensors* **2018**, *18*, 4092. https://doi.org/10.3390/s18124092.
42. Woebbecke, D.M.; Meyer, G.E.; Von Bargen, K.; Mortensen, D.A. Color indices for weed identification under various soil, residue, and lighting conditions. *Trans. ASAE* **1995**, *38*, 259–269. https://doi.org/10.13031/2013.27838.
43. Gitelson, A.A.; Kaufman, Y.J.; Stark, R.; Rundquist, D. Novel algorithms for remote estimation of vegetation fraction. *Remote Sens. Environ.* **2002**, *80*, 76–87. https://doi.org/10.1016/S0034-4257(01)00289-9.

44. Bendig, J.; Yu, K.; Aasen, H.; Bolten, A.; Bennertz, S.; Broscheit, J.; Gnyp, M.L.; Bareth, G. Combining UAV-based plant height from crop surface models, visible, and near infrared vegetation indices for biomass monitoring in barley. *Int. J. Appl. Earth Obs. Geoinf.* **2015**, *39*, 79–87. https://doi.org/10.1016/j.jag.2015.02.012.
45. Jang, G.; Kim, J.; Kim, D.; Chung, Y.S.; Kim, H.-J. Field Phenotyping of Plant Height in Kenaf (*Hibiscus cannabinus* L.) using UAV Imagery. *Korean J. Crop Sci.* **2022**, *67*, 274–284. https://doi.org/10.7740/kjcs.2022.67.4.274.
46. Administration, R.D. *Proper Fertilizer Use*; Rural Development Administration: Jeonju, Republic of Korea, 2022; Volume 42.
47. Authors, O. ODM—A Command Line Toolkit to Generate Maps, Point Clouds, 3D Models and DEMs from Drone, Balloon or Kite Images. Available online: https://github.com/OpenDroneMap/ODM (accessed on 7 June 2026).
48. DJI. *Mavic 3M Image Processing Guide*, version 1.0; DJI Agriculture: Shenzhen, China, 2023. Available online: https://dl.djicdn.com/downloads/DJI_Mavic_3_Enterprise/20230829/Mavic_3M_Image_Processing_Guide_EN.pdf (accessed on 26 April 2026).
49. QGIS Development Team. QGIS Geographic Information System; QGIS Association. 2023. Available online: http://qgis.org (accessed on 17 May 2026).
50. Rouse, J.W.; Haas, R.H.; Schell, J.A.; Deering, D.W. Monitoring vegetation systems in the Great Plains with ERTS. In *Proceedings of the ASA. Goddard Space Flight Center 3d ERTS-1 Symp.*; NASA STI: Hampton, VA, USA, 1974; Volume 351, p. 309.
51. Gitelson, A.A.; Kaufman, Y.J.; Merzlyak, M.N. Use of a green channel in remote sensing of global vegetation from EOS-MODIS. *Remote Sens. Environ.* **1996**, *58*, 289–298. https://doi.org/10.1016/S0034-4257(96)00072-7.
52. Louhaichi, M.; Borman, M.M.; Johnson, D.E. Spatially located platform and aerial photography for documentation of grazing impacts on wheat. *Geocarto Int.* **2001**, *16*, 65–70. https://doi.org/10.1080/10106040108542184.
53. Tucker, C.J. Red and photographic infrared linear combinations for monitoring vegetation. *Remote Sens. Environ.* **1979**, *8*, 127–150. https://doi.org/10.1016/0034-4257(79)90013-0.
54. R Core Team. *R: A Language and Environment for Statistical Computing*; R Foundation for Statistical Computing: Vienna, Austria, 2023. Available online: https://www.R-project.org (accessed on 17 May 2026).
55. Eom, T.S.; Kim, T.W.; Yoo, S.Y. Determination of Optimal Nitrogen Application Rates to Enhance Heat Stress Tolerance in Autumn Radish (*Raphanus sativus* L.) Using OJIP Transient Analysis. *Nitrogen* **2026**, *7*, 47. https://doi.org/10.3390/nitrogen7020047.
56. Zegada-Lizarazu, W.; Monti, A. Energy crops in rotation. A review. *Biomass Bioenergy* **2011**, *35*, 12–25. https://doi.org/10.1016/j.biombioe.2010.08.001.
57. Webber, C.L., III. Response of kenaf to nitrogen fertilization. In *Progress in New Crops*; Janick, J., Ed.; John Wiley & Sons: New York, NY, USA, **1996**; pp. 404–408.
58. Kuchinda, N.; Ndahi, W.; Lagoke, S.; Ahmed, M. The effects of nitrogen and period of weed interference on the fibre yield of kenaf (*Hibiscus cannabinus* L.) in the northern Guinea Savanna of Nigeria. *Crop Prot.* **2001**, *20*, 229–235. https://doi.org/10.1016/S0261-2194(00)00138-1.
59. Pushpa, K.; Murthy, N.K.; Murthy, R.K. Dry matter accumulation studies at different stages of crop growth in mesta (*Hibiscus cannabinus*). *Afr. J. Agric. Res.* **2013**, *8*, 332–338.
60. Duan, Q.; Liu, Q.; Yang, R.; Kong, X.; Gao, Y.; Yue, S.; Shen, Y.; Xu, M. Long-term co-application of nitrogen and organic fertilizers enhances soil quality and wheat growth stability by modulating microbial communities. *Appl. Soil Ecol.* **2025**, *213*, 106309. https://doi.org/10.1016/j.apsoil.2025.106309.
61. Sicignano, M.; Beleggia, R.; Del Piano, L.; Enotrio, T.; Suriano, S.; Raimo, F.; Trono, D. Effect of Combining Organic and Inorganic Fertilizers on the Growth of Hemp (*Cannabis sativa* L.) Plants and the Accumulation of Phytochemicals in Their Inflorescence. *Plants* **2025**, *14*, 1519. https://doi.org/10.3390/plants14101519.
62. Taiz, L.; Zeiger, E.; Møller, I.M.; Murphy, A. *Plant Physiology and Development*, 6th ed.; Sinauer Associates, Inc.: Sunderland, MA, USA, **2014**.
63. Ruiz, A.; Listello, A.; Trifunovic, S.; Archontoulis, S.V. Maize breeding enhances lodging resistance through vertical allocation changes of stem dry matter and nitrogen. *Front. Plant Sci.* **2025**, *16*, 1514045. https://doi.org/10.3389/fpls.2025.1514045.
64. Berry, P.; Sterling, M.; Spink, J.; Baker, C.; Sylvester-Bradley, R.; Mooney, S.; Tams, A.; Ennos, A. Understanding and reducing lodging in cereals. *Adv. Agron.* **2004**, *84*, 215–269.
65. Shah, L.; Yahya, M.; Shah, S.M.A.; Nadeem, M.; Ali, A.; Ali, A.; Wang, J.; Riaz, M.W.; Rehman, S.; Wu, W. Improving lodging resistance: Using wheat and rice as classical examples. *Int. J. Mol. Sci.* **2019**, *20*, 4211. https://doi.org/10.3390/ijms20174211.

66. Cabrera-Bosquet, L.; Molero, G.; Stellacci, A.; Bort, J.; Nogués, S.; Araus, J. NDVI as a potential tool for predicting biomass, plant nitrogen content and growth in wheat genotypes subjected to different water and nitrogen conditions. *Cereal Res. Commun.* **2011**, *39*, 147–159. https://doi.org/10.1556/crc.39.2011.1.15.
67. Rehman, T.H.; Lundy, M.E.; Linquist, B.A. Comparative sensitivity of vegetation indices measured via proximal and aerial sensors for assessing N status and predicting grain yield in rice cropping systems. *Remote Sens.* **2022**, *14*, 2770. https://doi.org/10.3390/rs14122770.
68. Xue, J.; Su, B. Significant remote sensing vegetation indices: A review of developments and applications. *J. Sens.* **2017**, *2017*, 1353691. https://doi.org/10.1155/2017/1353691.
69. Lee, S.-J.; Han, S.-W.; Kim, T.-W.; Yoo, S.-Y. RGB image-based drought stress classification of garden plants using SVM model. *Sci. Rep.* **2026**, *16*, 21087. https://doi.org/10.1038/s41598-026-51726-1.
70. Bannari, A.; Morin, D.; Bonn, F.; Huete, A. A review of vegetation indices. *Remote Sens. Rev.* **1995**, *13*, 95–120. https://doi.org/10.1080/02757259509532298.
71. Wang, S.; Yang, D.; Li, Z.; Liu, L.; Huang, C.; Zhang, L. A global sensitivity analysis of commonly used satellite-derived vegetation indices for homogeneous canopies based on model simulation and random forest learning. *Remote Sens.* **2019**, *11*, 2547. https://doi.org/10.3390/rs11212547.
72. Besic, N.; Picard, N.; Vega, C.; Bontemps, J.-D.; Hertzog, L.; Renaud, J.-P.; Fogel, F.; Schwartz, M.; Pellissier-Tanon, A.; Destouet, G. Remote-sensing-based forest canopy height mapping: Some models are useful, but might they provide us with even more insights when combined? *Geosci. Model. Dev.* **2025**, *18*, 337–359. https://doi.org/10.5194/gmd-18-337-2025.
73. Ouyang, J.; De Bei, R.; Fuentes, S.; Collins, C. UAV and ground-based imagery analysis detects canopy structure changes after canopy management applications. *OENO One* **2020**, *54*, 1093–1103. https://doi.org/10.20870/oeno-one.2020.54.4.3647.
74. Biswal, S.; Pathak, N.; Chatterjee, C.; Mailapalli, D.R. Estimation of aboveground biomass from spectral and textural characteristics of paddy crop using UAV-multispectral images and machine learning techniques. *Geocarto Int.* **2024**, *39*, 2364725. https://doi.org/10.1080/10106049.2024.2364725.
75. Awichin, P.; Laosuwan, T.; Sangpradid, S.; Uttaruk, Y.; Phoophathong, T.; Leammanee, S.; Nuchthapho, J. UAV multispectral indices and linear regression for estimating biomass and carbon in rubber plantations. *IEEE Access* **2025**, *13*, 215845–215865. https://doi.org/10.1109/ACCESS.2025.3644408.
76. Shi, J.; Yang, K.; Yuan, N.; Li, Y.; Ma, L.; Liu, Y.; Fang, S.; Peng, Y.; Zhu, R.; Wu, X. UAV-based rice aboveground biomass estimation using a random forest model with multi-organ feature selection. *Eur. J. Agron.* **2025**, *164*, 127529. https://doi.org/10.1016/j.eja.2025.127529.
77. Radoglou-Grammatikis, P.; Sarigiannidis, P.; Lagkas, T.; Moscholios, I. A compilation of UAV applications for precision agriculture. *Comput. Netw.* **2020**, *172*, 107148. https://doi.org/10.1016/j.comnet.2020.107148.
78. Yang, X.; Chen, J.; Lu, X.; Liu, H.; Liu, Y.; Bai, X.; Qian, L.; Zhang, Z. Advances in UAV remote sensing for monitoring crop water and nutrient status: Modeling methods, influencing factors, and challenges. *Plants* **2025**, *14*, 2544. https://doi.org/10.3390/plants14162544.